Synthesis and characterization of doped nano-sized ceria–zirconia solid solutions

Xiaole Weng [a,b], Ben Perston [c], Xue Z. Wang [c], Isaac Abrahams [d], Tian Lin [a], Shoufeng Yang [b], Julian R.G. Evans [a], David J. Morgan [e], Albert F. Carley [e], Michael Bowker [e], Jonathan C. Knowles [f], Ihtesham Rehman [b], Jawwad A. Darr [a,*]

[a] Department of Chemistry, University College London, Christopher Ingold Laboratories, 20 Gordon Street, London WC1H 0AJ, UK
[b] The School of Engineering and Materials Science, Queen Mary University of London, Mile End Road, London, E1 4NS, UK
[c] Institute of Particle Science & Engineering, School of Process, Environmental and Materials Engineering, University of Leeds, Clarendon Road, Leeds LS2 9JT. UK
[d] Centre for Materials Research, School of Biological and Chemical Sciences, Queen Mary University of London, Mile End Road, London, E1 4NS, UK
[e] School of Chemistry, Cardiff University, Main Building, Park Place, Cardiff, CF10 3AT, UK
[f] Division of Biomaterials and Tissue Engineering, UCL Eastman Dental Institute, University College London, 256 Gray's Inn Road, London, WC1X 8LD. UK

ARTICLE INFO

ABSTRACT

Two compositions $Ce_{0.50}Zr_{0.39}La_{0.04}Y_{0.07}O_{2-\delta}$ and $Ce_{0.25}Zr_{0.65}La_{0.04}Y_{0.06}O_{2-\delta}$ based on ceria-zirconia solid solutions were prepared as nanopowders using a continuous hydrothermal flow synthesis reactor, followed by either freeze-drying or hotplate-drying of the slurry. Each dried nanopowder was then subjected to 10 h heat-treatment at 1000 °C, 1100 °C or 1200 °C in air (to simulate accelerated ageing). The reducibility and hydrogen consumption of the oxidised samples were measured using temperature programmed reduction (TPR) up to 1000 °C. The effects of composition, drying method and heat-treatment temperature were evaluated on the TPR profiles of the materials. The powders were further investigated using a range of analytical methods including UV/Vis spectroscopy (which yielded colour data), Raman spectroscopy, powder X-ray diffraction, BET surface area measurements and X-ray photoelectron spectroscopy (XPS). Chemometric methods were used to investigate relationships between the spectroscopic and total oxygen storage capacity (OSC) data. Principal component analysis (PCA) was used to provide a simple interpretation of the effects of various synthesis and treatment parameters on Raman spectra. Principal component regression (PCR) was used to build regression models relating the Raman spectra and the temperature of hydrogen consumption peak at several set temperatures in the TPR. The total hydrogen consumption of the materials was generally high, while the drying and heat-treatment conditions appeared to have a significant effect on the final properties of the resulting powders, such as the surface area and total oxygen storage capacity.

© 2009 Elsevier B.V. All rights reserved.

1. Introduction

Catalytic reduction of pollutants from automotive exhausts represents one of the major applications of heterogeneous catalysis today [1]. Currently, >90% of new gasoline fuelled cars sold in the world are equipped with catalytic converters based on the principle of three way catalysis (TWCs) [2]. So called TWCs are designed simultaneously to convert emissions of CO, hydrocarbons and NO_x, into relatively harmless products of CO_2, H_2O and N_2 under a range of engine conditions [3]. Towards the development of better TWCs, a number of support materials with high oxygen storage capacity (OSC) have been investigated, particularly based on the doped ceria fluorite lattice. The OSC is an important property of TWC materials enabling them to cope with a range of air–fuel ratios, being either fuel-rich (reducing) or fuel-lean (oxidizing) conditions [4]. Ceria-containing fluorite based materials can cope with such fluctuations by virtue of the formation of Ce^{3+} in fuel-rich regimes and its conversion to Ce^{4+} in fuel-lean circumstances. The addition of platinum group metals, (PGM, e.g. Pt, or Pd or Rh), at <1 wt% levels on the surface of the ceria-containing material can reduce the light-off temperature (temperature required to produce activated oxygen) by hundreds of degrees centigrade and promote NO_x reduction [5].

Thermal stability of oxygen storage materials is highly desirable for current TWC applications since the operating temperature can reach >1000 °C in a close-coupled converter [1,6]. In order to meet these requirements, vehicle manufacturers often perform accelerated ageing tests [7]. Indeed, the biggest problem for poor performance or deactivation of TWCs is the loss of properties as a

result of ageing in use. This can occur due to the following reasons; (i) sintering of the materials giving low surface area and less labile oxygen, (ii) thermal destabilization of the OSC materials and (iii) deactivation of the PGM (this can also be from sintering), which affects the light-off temperature.

Historically, early TWC materials such as those based on ceria alone showed poor thermal stability, which was to some extent improved through the use of dopants such as zirconia, i.e. to form ceria–zirconia solid solutions with the general formula $Ce_xZr_{1-x}O_{2-\delta}$ (CZ) [8–10]. Thereafter, sintering of such materials was addressed in third generation TWCs through the introduction of alumina particles to prevent sintering of the ceria–zirconia grains [11]. This approach seemed to be fruitful and led to improvements in OSC, durability and overall catalytic performance. Other doped ceria materials of interest for TWC materials, include Ce–Pr oxides (CP) [12,13], Ce–Zr–Pr oxides (CZP) [13–16]. Ce–Zr–Nd oxides (CZN) [13,17] and more recently, Ce–Zr–La oxides (CK) [18].

Several underlying themes seem to exist in the desirable attributes of the TWC materials; they need to be active at low temperatures, be durable, retain a high surface area after accelerated ageing and possess a high OSC under fuel-rich or fuel-lean conditions. The following factors have a strong influence on performance of CZ based TWCs (ignoring the effects of a PGM or other wash-coat or surface coatings for a moment): (i) the precipitation method used, (ii) the use of dopants in the lattice (iii) the structure of the oxide sublattice and defects associated with solid solution formation, (iv) the drying procedure, (v) the heat-treatment regimes used for the final material (including thermal history) and (vi) the conditions used for durability tests.

A number of different synthesis methods have been reported for the production of fluorite phase doped ceria directed towards TWC applications, e.g. by ball milling [19], room temperature co-precipitation [20–23], combustion syntheses [24–26], sol–gel syntheses [27–29]. Several of these processes do not afford good homogenous doping, or give low surface area materials and poor oxygen lability. More low temperature labile oxygen and a greater total OSC are believed to be obtained when there is a truly random (homogenous) distribution of Ce^{4+} and Zr^{4+} cations in the oxide lattice (and possibly other M^{3+} dopants) [30]. This is due to the creation of oxide ion vacancies and a more defective fluorite structure. Hence, synthetic routes, which offer homogenous doping of the ceria lattice with high surface area (and a small crystallite size), are very much of interest in this regard.

A number of nanomaterial synthesis methods have recently been developed, which exploit the unusual properties of super-critical (sc) fluids (these properties include enhanced diffusivity, rapid reaction kinetics, controllable solvent properties). Such fluids are essentially single phase pure substances which are above the critical temperature and pressure for that substance, the most popular of which are sc-water [9,10,31–35] and sc-CO₂ [36–47], respectively. Supercritical (and sub-critical) water have been used in batch hydrothermal processes for the syntheses of inorganic materials [48–55], however, such processes have limitations in that reaction parameters and particle properties are not easy to control, resulting in poor particle reproducibility. Hence, continuous hydrothermal processes for particle synthesis are very much of interest as they offer greater control as reaction parameters can be modulated in flow and there is less opportunity for grain growth compared to batch processes. This allows high surface area powders to be readily produced [9,10,31–35].

Following pioneering research of the Arai Group in Japan in the early nineties to develop continuous hydrothermal reactors [48,56–58], Poliakoff and co-workers first reported the use of a continuous hydrothermal (using supercritical water) flow synthesis (CHFS) method in 2000 for the synthesis of homogenous CZ

solid solutions [9,10] The CHFS process effectively involves mixing a solution containing one or more metal salts meeting with a stream of supercritical (or superheated) water, where upon rapid nucleation of very high surface area nano-sized crystallites occurs in a matter of seconds at below 400 °C and 24.1 MPa (such as the reported nominal 50:50 CZ which had a BET surface area of ca. 180 m² g⁻¹). Subsequently, the authors used this technology for the synthesis of several useful nanomaterials [31–35]. Recently, Korean researchers in collaboration with Hanwa Corporation of Korea revisited this area using an analogous continuous hydro-thermal process and reported the OSC of the CZ nanomaterials [59]. Such materials showed excellent behaviour with labile oxygen reported at relatively low temperatures. However, the work did not reveal any insights into the properties of such materials after accelerated ageing at very high temperatures (≥1000 °C).

In this work, we have synthesized two Ce–Zr–La–Y oxide solid solutions with different compositions. Small amounts of La^{3+} and Y^{3+} cations were doped into the solid solutions with a view to introducing oxide ion vacancies and structural defects into the respective fluorite CZ lattices [18,60]. The effects of drying and post synthesis heat-treatment temperature on the TPR hydrogen consumption values, were studied. Chemometrics were applied to the data to investigate any significant correlations between the measured surface areas, TPR profiles and spectroscopic data.

2. Experimental details

2.1. Materials

[Y(NO₃)₃·6H₂O, ≥99.9%], [Ce(NH₄)₂(NO₃)₆, ≥98.5%], [La(NO₃)₃ ·6H₂O, ≥99%] and [ZrO(NO₃)₂·6H₂O, ≥99%] were supplied by Sigma–Aldrich Chemical Company (Dorset, UK). Potassium hydro-xide pellets (KOH, ≥85%) supplied by VWR International (Leices-tershire, UK) were used to adjust the pH. Hydrogen peroxide liquid (H₂O₂, 30 vol%) supplied by VWR international (Leicestershire, UK) was used to increase the yield. For TPR experiments H₂ was used as obtained (BOC, 5% H₂ in Argon). All chemicals were used as obtained.

2.2. General syntheses

The as-prepared products were manufactured in our labora-tory using a three pump-hydrothermal flow system (CHFS) [34]. The reactor, tubing and components were all made of 316 stainless steel (Swagelok™). The apparatus (Fig. 1) consists of a metal salt(s) solution HPLC pump, P2 (Gilson model 305/25 SC pump head), a base solution HPLC pump, P3 (Gilson model 305/25 SC pump head) and a water HPLC pump, P1 (Gilson model 305/25 SC pump head). Water was pumped through an electrical pre-heating coil (2.5 kW) and heated to the appropriate temperature (450 °C). Flow rates of 10, 10 and 20 mL min⁻¹, were used for the metal salt solution, base solution and water stream, respectively. The system pressure was maintained at 24.1 MPa by a Tescom back-pressure regulator (BPR) Model 26-1762-24-194. The products were $Ce_{0.50}Zr_{0.39}La_{0.04}Y_{0.07}O_{2-\delta}$ and $Ce_{0.25}Zr_{0.65}La_{0.04}Y_{0.06}O_{2-\delta}$, hereby referred to as 50CeDT and 25CeDT (where T = heat-treatment temperature in degrees centigrade or T = A for as-prepared with no heat-treatment; D = H or F for hotplate-dried or freeze-dried, respectively).

For the synthesis of 50CeDT, ammonium cerium nitrate (27.32 g, 50.0 mmol), zirconyl nitrate hexahydrate (8.05 g, 24.0 mmol), lanthanum nitrate hexahydrate (1.90 g, 4.0 mmol) and yttrium nitrate hexahydrate (2.43 g, 6.0 mmol) were all dissolved in 900 mL of DI water to give concentrations of 55 mM, 26 mM, 5 mM and 7 mM, respectively. 90 mL of H₂O₂ liquid (10 vol%) was added to the solution, which was first pumped and
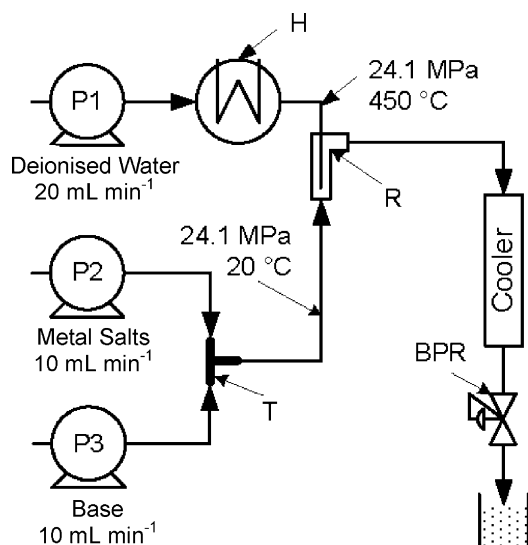
Fig. 1. Schematic representation of the three-pump continuous hydrothermal flow synthesis system used for the preparation of nanoparticles. Key: P = HPLC pump, C = cooling, F = filter, B = back-pressure regulator, R = counter-current mixer, T = Tee-piece mixer and H = water pre-heater. Additional band heater (on the counter-current mixer) and filter (between the cooler and BPR) omitted for clarity.

brought to mix in a stainless steel Swagelok^{TM} 1/8″ "Tee" piece (T, see Fig. 1) with a potassium hydroxide solution to give a pH of 14. The superheated water feed was then brought into contact with this mixture using a vertical coaxial counter-current mixing arrangement as described elsewhere [62]. The mixing point was made from Swagelok^{TM} parts and a band heater set to 450 °C (200 W Watlow band heater) was added to maintain the reaction temperature as described recently [33]. The suspensions were cooled and then passed through a 7 μm filter (F) to remove any larger aggregates that might affect smooth operation, of the back-pressure regulator (BPR). Solids were recovered from the exit of the BPR and then cleaned by centrifuging the suspension (30 min at 4500 rpm), decanting the liquid phase and washing the solids thoroughly with clean water. This procedure was repeated once more, ca. 40 mL of liquid phase was decanted and the concentrated slurry was dried by either freeze-drying or hotplate-drying. Freeze-drying was performed using a Vertis Advantage freeze-dryer at 133 MPa for a period of 22.5 h. Hotplate-drying was performed by taking a 100 mL slurry in a 500 mL glass beaker and then heating it on a hotplate (RET basic C, IKA®WERKE) at 120 °C

overnight. According to the dried mass, the yield was calculated as ca. 84% for 50CeDA materials. For heat-treatments, the powders were placed in a Lenton muffle furnace (UAF18/5) for 10 h (dwelling time) in air at 1000 °C, 1100 °C and 1200 °C, respectively, with a heating rate of 10 °C min^{-1} from room temperature. Samples of approximately 0.5 g were each spread evenly onto a platinum plate in the furnace.

For the syntheses of 25CeDT materials, ammonium cerium nitrate (12.31 g, 22.0 mmol), zirconyl nitrate hydrate (14.50 g, 43.0 mmol), lanthanum nitrate hexahydrate (1.71 g, 4.0 mmol) and yttrium nitrate hexahydrate (2.19 g, 6.0 mmol), were dissolved in 900 mL of DI water to give concentrations of 25 mM, 48 mM, 4 mM and 6 mM, respectively. Thereafter, the synthesis was conducted under identical conditions. The products were then either freeze-dried or hotplate-dried and subsequent heat-treatments were also conducted (see Table 1). The yield based on dry mass was calculated at ca. 64 % for 25CeDA samples.

2.3. Methods and equipment for characterization

10 MΩ deionized (DI) water from a USF Elga water deionizer was used throughout. Gilson model 305 HPLC pumps were used in the CHFS system. Freeze-drying was performed using a Vitris Advantage Freeze Dryer, Model 2.0 ES, supplied by BioPharma; the solids were frozen in liquid nitrogen and then freeze-dried for 22.5 h at 133 Pa. The molar elemental composition Ce:Zr:Y:La of the products was measured using an Oxford Instruments Inca 400 EDX detector connected to a scanning electron microscope (JEOL 5410 LZSEM). Averages of 10 area scans (1 × 1 μm areas) were used to calculate average elemental compositions. Particle size and morphology of the as-prepared samples were investigated using a HR-TEM model JEOL 4000EX high-resolution transmission electron microscope (400 kV accelerating voltage). Samples were collected on carbon-coated copper grids (Holey Carbon Film, 300 meshes Cu, Agar Scientific, Essex, UK) after being briefly dispersed ultrasonically in methanol (Kerry^{TM} Ultrasonic bath, Skipton, UK) for 3 min. BET surface area measurements (multipoint) were performed on a Micromeritics Gemini analyzer. All powders were degassed at 80 °C for 2 h prior to BET analysis. X-ray powder diffraction studies were conducted on a Siemens D5000 X-ray diffractometer using Cu-Kα radiation (λ = 0.15418 nm). Data were collected over the 2θ range 20–70° with a step size of 0.02° and a count time of 10 s per step. The diffraction patterns were analyzed by Rietveld refinement using GSAS [61]. A Nicolet Almega Dispersive Raman Spectrometer (532 nm) was used in the wavenumber range 200–800 cm^{-1} averaging 20 scans for 20 s

Table 1
Fit parameters (pseudo-Voigt) for the Miller indices peak, the corresponding grain size and strain estimated by applying a modified Scherrer method as well as the redox percentage for the respective samples.

Sample	Identity	Angle (2θ) (°)	FWHM (2θ) (°)	Grain size (nm)	Microstrain	Surface area (m² g^{-1})	Redox (%)
S1	25CeFA	29.53	1.96	5.4	0.023	189.5	98.6
S2	25CeF1000	29.56	0.23	31.3	0.0018	5.5	103.9
S3	25CeF1100	29.56	0.17	67.5	0.0021	<1.0	101.6
S4	25CeF1200	29.59	0.12	124.5	0.0017	<1.0	107.0
55	25CeHA	29.52	1.96	6.1	0.024	190.7	94.2
S6	25CeH1000	29.56	0.23	32.7	0.0018	5.3	103.1
S7	25CeH1100	29.57	0.17	69.6	0.002	1.8	98.7
S8	25CeH1200	29.57	0.15	194.9	0.0023	<1.0	96.3
S9	50CeFA	29.03	2.01	6.1	0.0256	185.0	69.1
S10	50CeF1000	29.05	0.40	16.9	0.0025	13.8	72.6
S11	50CeF1100	29.07	0.17	51.4	0.0018	2.2	72.0
S12	50CeF1200	29.07	0.15	72.7	0.0017	<1.0	71.4
S13	50CeHA	29.03	2.00	5.8	0.0249	183.8	68.3
S14	50CeH1000	29.06	0.32	21.6	0.0024	6.8	74.0
S15	50CeH1100	29.07	0.20	45.9	0.0021	1.4	82.8
S16	50CeH1200	29.09	0.16	104.0	0.0023	<1.0	70.3

Note: F = freeze-dried; H = hotplate-dried and samples were all heated for 10 h in air; A = as-prepared.

each. Colour measurements for all samples were recorded using a Perkin Elmer (Lambda 950) UV–vis spectrophotometer with an integrating sphere accessory by the diffuse reflectance method and were analyzed by using COLOR® software (Perkin Elmer, UK). The UV–Vis data were recorded in the range 320 to 800 nm using Spectralon blank as reflecting standard and a D65 standard illuminant with a $10°$ viewing angle. The chromatic coordinates of the samples were recorded. The X-ray photoelectron spectroscopy (XPS) experiments were performed on a Kratos Axis Ultra-DLD photoelectron spectrometer using monochromatic Al-Kα radiation (photon energy 1486.6 eV). Survey scans were performed at a pass energy (PE) of 160 eV, whilst detailed scans were performed at PE 40 eV. All data were analyzed using CasaXPS™ software (Version 2.3.14). All data were calibrated to the C(1s) signal, which was assigned a value of 284.7 eV, and attributable to adventitious carbon. Curve fits were performed using a linear background and a Gaussian peak shape with 30% Lorentzian character.

The details of the TPR test and equipment were as follows. The instrument was an AMI-30 supplied by Altamira Instruments, Pittsburgh, USA. Samples size was 0.1 g of mixed oxide powder placed in a 'U' shaped cell and held in position with silica wool. The TPR test method used the following steps: 1. (pre-treatment/oxidation step), in which samples were heated to 400 °C with a dwell of 20 min and then cooled to 100 °C. The process was operated with a purge of flowing O_2/He (10% O_2 in helium) gas at the rate of 25 mL min^{-1}. The ramp rate was controlled at 30 °C min^{-1}. Step 2 (TPR step): Samples were heated up to 1000 °C at 10 °C min^{-1} with a dwell time of 1 h under flowing H_2/Ar (5 % H_2 in Argon) at 25 mL min^{-1} and then cooled to 100 °C. The change in thermal conductivity of gas before and after sample was recorded throughout this step. Steps 1 and 2 were repeated. The data from the second TPR cycle was used for analysis. The peak of thermal conductivity detector (TCD) signal was reported as the low temperature reduction peak and integrated against time (equate to temperature). This result was compared to a standard (Cu oxide supplied from Sigma–Aldrich, Dorset UK, ≥99.9%) to give H_2 consumption as a function of temperature (units are H_2 μmols g^{-1} catalysis).

3. Results and discussion

3.1. Phase characterizations and BET measurements

The constitutional molar ratios of the as-prepared products were evaluated using calibrated EDX, and gave Ce:Zr:La:Y molar ratios for 50CeFA and 25CeFA as $Ce_{0.50}Zr_{0.39}La_{0.04}Y_{0.07}O_{2-\delta}$ and $Ce_{0.25}Zr_{0.65}La_{0.04}Y_{0.06}O_{2-\delta}$, respectively, which slightly deviated from the precursor stoichiometries of $Ce_{0.59}Zr_{0.28}La_{0.05}Y_{0.08}O_{2-\delta}$ and $Ce_{0.30}Zr_{0.57}La_{0.05}Y_{0.08}O_{2-\delta}$. This deviation is due to differences in the kinetics of precipitation for the different precursor species and is related to the fact that the time for such precipitation is in a few seconds in the reactor rather than a few hours. The particle morphologies of as-prepared 50CeFA samples were analyzed using high-resolution TEM images that showed rounded plate-like highly crystalline agglomerated particles with a mean particle size of 4.5 ± 0.8 nm (range 2.8–6.0 nm, Fig. 2).

Phase identities and purities of the samples, which were denoted from S1 to S16 (see Table 1 for thermal histories of the samples) were elucidated using X-ray powder diffraction (XRD) and Raman spectroscopy. The XRD patterns of all samples are shown in Fig. 3. To aid comparison, the XRD patterns are grouped by sample composition (rather than sequence "S" number) and also by the heat-treatment temperature used. The symmetrical peaks of these samples were consistent with the characteristic peaks of either cubic CeO_2 or tetragonal ZrO_2, suggesting the formation of a solid solution. The characteristic peaks for 50CeDT
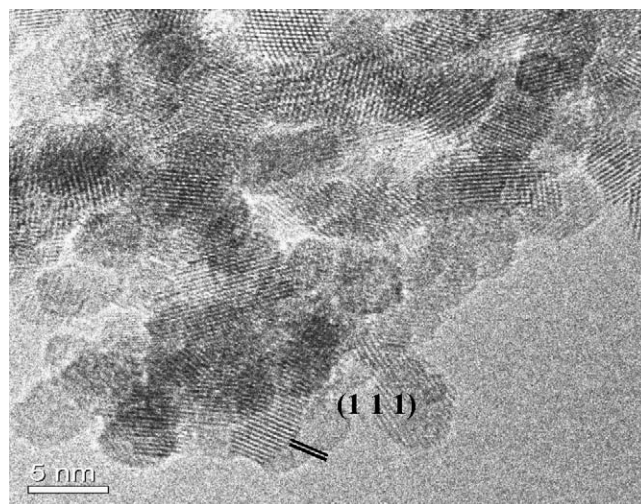

Fig. 2. Transmission electron microscope images (5×10^5 magnification) of sample 50CeFA (bar = 5 nm) made in the continuous hydrothermal flow synthesis system, using a superheated water feed at 450 °C and 24.1 MPa and a Ce:Zr:La:Y solution ratio of 523:365:46:66, respectively. The lattice space measured from the fringes in TEM at 0.53 ± 0.6 nm (range 0.47–0.59 nm based on 20 fringes, which is close to the values calculated using XRD refinement).

plots shifted to larger two theta angles compared to 25CeDT plots. This is due to a contraction of the lattice cell parameter by the insertion of more ZrO_2 (ionic radius of Zr^{4+} = 0.087 nm [13]) into the CeO_2 fluorite lattice (ionic radius of Ce^{4+} = 0.097 nm [13]) in the 25CeDT samples [59]. This is further confirmed by the unit cell parameter calculation (see below). As expected, the XRD data for all samples gave increasingly sharp peaks with increasing heat-treatment temperatures. After heat-treatment of the 25CeDA samples at either 1000 °C, 1100 °C or 1200 °C, there was a general increase in the degree of tetragonal distortion, i.e. splitting of the
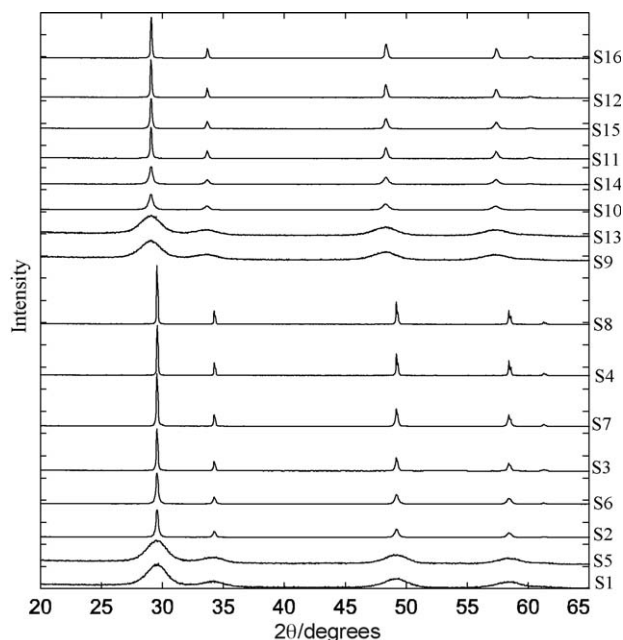

Fig. 3. XRD plots for all as-prepared and heat-treated samples. From bottom, the order is 25CeFA (S1, magnified ×5), 25CeHA (S5, ×5), 25CeF1000 (S2), 25CeH1000 (S6), 25CeF1100 (S3), 25CeH1100 (S7), 25CeF1200 (S4), 25CeH1200 (S8), 50CeFA (S9, ×5), 50CeHA (S13, ×5), 50CeF1000 (S10), 50CeH1000 (S14), 50CeF1100 (S11), 50CeH1100 (S15), 50CeF1200 (S12), 50CeH1200 (S16), where H = hotplate-dried; F = freeze-dried and T = either as-prepared (A) or heat-treated (H) at the indicated temperature for 10 h.
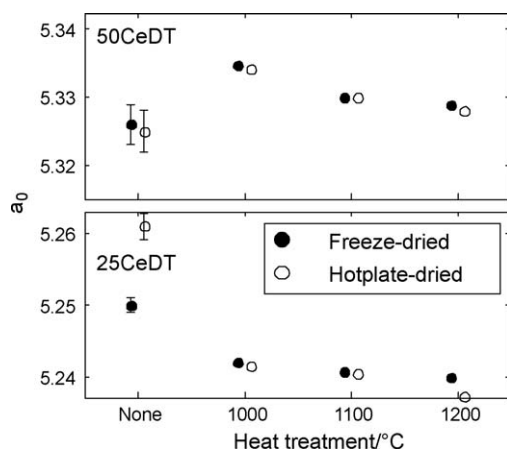
Fig. 4. Unit cell parameter plot versus heat-treatment temperatures for 25CeDT and 50CeDT samples. For the heat-treated samples (H), the error bars (not shown) are smaller than the plot symbols.

peaks at $2\theta = 49°$ and $58°$, was observed in the XRD data. No similar XRD peak splitting was observed for the 50CeDA samples after such heat-treatments, indicating that the cubic structure was stable for this composition under the heat-treatment tests, suggesting that the 50CeDA starting materials (S9 and S13) made by CHFS did indeed possess high homogeneity.

Unit cell parameters were calculated based on a cubic phase for the 50CeDT and 25CeDT samples and are presented in Fig. 4. Heat-treatment of the 25CeDA samples led to a slight lattice contraction, which could be due to; (i) a loss of oxide ions due to an increase in trivalent cation segregation on the surface or (ii) partial oxidation of Ce^{3+} (larger radius at 0.114 nm [13]) to Ce^{4+}. For the 50CeD1000 samples (S10 and S14), an increase in the lattice parameter was observed compared to the corresponding as-prepared analogues (50CeDA; S9 and S13). This might not reveal an actual expansion in the lattice, since broad XRD peaks were obtained for the as-prepared samples, which induced a comparatively large error for them during refinement. Upon increasing the heat-treatment temperature for the 50CeDT samples, a contraction of the lattice was observed, which could be explained by similar reasons to those given above.

Crystallite sizes of all samples were estimated using XRD peak full peak widths at half maximum height (applying the Scherrer equation). The results are summarized in Table 1. A progressive increase in crystallite size from 5 nm to ca. 190 nm due to the heat-

treatments was observed and consequently, the surface areas of heat-treated samples were reduced (see Table 1). Microstrain values, which in this case reflect the variation in lattice parameter caused by the forces exerted between grains during synthesis, are seen to decrease by around an order of magnitude after initial heat-treatment. The values obtained post thermal treatment are consistent with a homogenous solid solution.

BET surface areas of the CHFS samples were strongly dependant upon the initial conditions of synthesis and the heat-treatment temperatures (used to simulate accelerated ageing). Heat-treatment parameters for the samples were chosen as a heating/cooling ramp rate of 10/20 °C min^{-1}, respectively and holding at the target temperature for 10 h at either 1000 °C, 1100 °C and 1200 °C. The as-prepared 25CeDA and 50CeDA samples (S1, S5, S9 and S13), had BET surface areas in the relatively narrow range 184.0–190.0 $m^2 g^{-1}$. This is not consistent with our previous work, which had suggested that for other ceramics, freeze-drying may be expected to result in significantly higher BET surface areas compared to direct hotplate-drying methods [63].

The 25CeD1200 and 50CeD1200 samples (S4, S8, S12 and S16) had BET surface areas $< 1 m^2 g^{-1}$, which was lower than expected, but can be explained by the high sinterability of the initial nanocrystalline powders. In contrast, the 25CeD1100 and 50CeD1100 samples had marginally higher surface areas in the range from $< 1 m^2 g^{-1}$ to 2.2 $m^2 g^{-1}$ for 25CeD1000 whilst the 50CeD1000 samples (S2, S6, S10 and S14) had surface areas in the range 5.3 $m^2 g^{-1}$ to 13.8 $m^2 g^{-1}$, with S10 (50CeF1000) having the highest value. In comparison, the hotplate-dried sample S14 (50CeH1000), had a surface area of 6.8 $m^2 g^{-1}$ after being heat-treated under identical conditions to S10. Evidently, for this particular composition, the different drying methods had a significant effect on the sintering behaviour, and as will be seen later, this in turn gave different oxygen release profiles for compositionally identical materials.

XRD data for the as-prepared 25CeDA and 50CeDA samples (S1, S5, S9 and S13) showed only broad peaks making actual phase assignments difficult, consequently, Raman spectroscopy was used to identify the structures. The Raman spectra revealed that S9 (50CeFA) and S13 (50CeHA) were cubic phase as a result of a single prominent peak at ca. 480 cm^{-1}, assigned to the F_{2g} Raman active mode of the fluorite-like structure (Fig. 5b) [18]. This peak was shifted to ca. 493 cm^{-1} upon heat-treatment to 1200 °C, associated with the increase in crystallite size (see Table 1). The presence of a broad peak at ca. 286 cm^{-1}, which became more intense with heat-treatment, generally originated from the displacement of oxygen atoms from their ideal fluorite lattices [64]. Another broad peak was
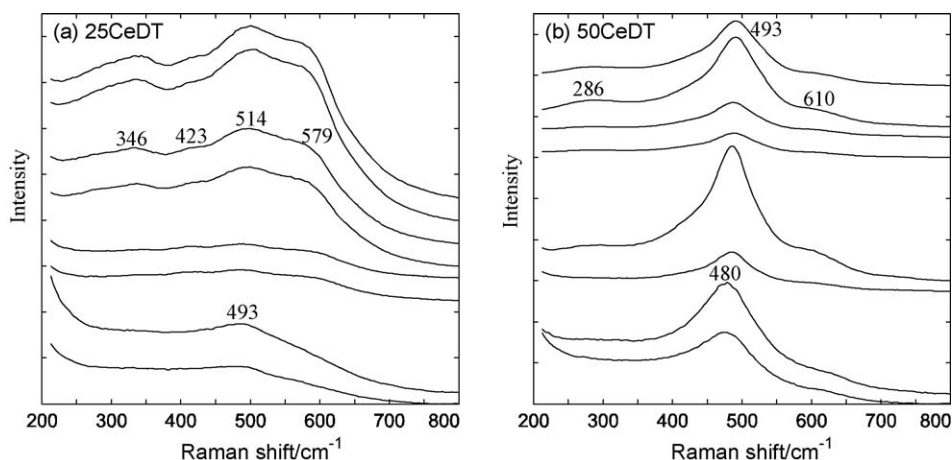

Fig. 5. Raman spectra of as-prepared and heat-treated samples for (a) the 25CeDT series and (b) 50CeDT series. The spectra are offset for clarity; the order, in each plot and from bottom, is FA, HA, F1000, H1000, F1100, H1100, F1200, H1200. In panel (b) the DA spectra have been magnified by ×20 and the D1000 spectra by ×10.

observed at ca. 610 cm^{-1} which was from the longitudinal optical (LO) mode of ceria as reported in the literature elsewhere [65,66].

For all 50CeDT samples, the Raman analysis (as well as XRD results) suggested the samples were cubic phase, even after heat-treatments. The Raman data for the 25CeDA samples (S1 and S5) only revealed one very broad peak at ca. 493 cm^{-1}, suggesting a possible cubic phase had been obtained (Fig. 5a). After heat-treatment of these samples to 1000 °C, broad peaks were obtained for sample S2 and S6 (25CeD1000), possibly suggesting the material was tetragonal (or contained a tetragonal phase). This is in agreement with the corresponding XRD data. After heat-treatment of the 25CeDA samples to 1100 °C (25CeD1100), the Raman spectra revealed four broad peaks at ca. 346, 423, 514 and 579 cm^{-1}, suggesting that a "pseudo-cubic t" phase was obtained. The strong peak at 514 cm^{-1} was assigned to the F_{2g} Raman active mode of the fluorite-like structure, which is weakened when more oxygen vacancies are created [13]. The Raman bands at 346, 423 cm^{-1} are believed due to the defect species that contain oxygen vacancies whilst the peak at 579 cm^{-1} is attributed to the presence of defect species including dopant cations, but not oxide ion vacancies [67]. Similarly, for the 25CeD1200 samples, the material was assumed to be the "pseudo-cubic t" phase on the basis of Raman data. These results are consistent with conclusions of the afore mentioned XRD data.

The effect of different drying methods on Raman spectra was investigated using principal components analysis (PCA), which is a chemometric technique for reducing the dimensionality of datasets with many correlated variables, approximating them with a smaller set of uncorrelated principal components (PCs) [68]. PCA is particularly useful in spectroscopy, where there may be hundreds or thousands of wavelength variables that are very strongly correlated. The PCs can provide a more readily interpretable summary of the data and may also be used as uncorrelated predictor variables in regression. The PCA in this work was carried out using the PLS_Toolbox version 4 (Eigenvector Research, Wenatchee, WA) running under MATLAB version 7.0.1 (The Mathworks, Natick, MA).

Fig. 6 shows the scores on the first two PCs of the Raman dataset, calculated after constant baseline subtraction and normalization of the spectra to unit maximum intensity. The two
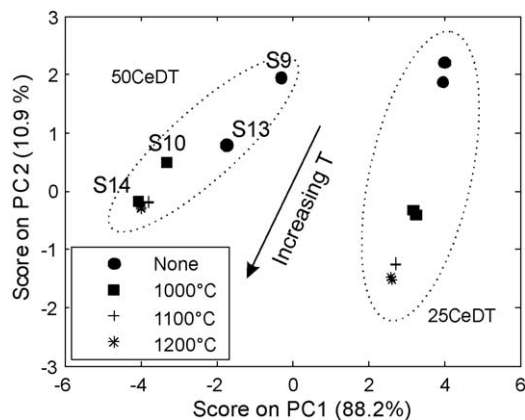
Fig. 6. Principal components analysis of normalized Raman spectra. The 306 Raman-shift frequency variables have been compressed into two principal components to facilitate plotting and interpretation.

compositions of material form clusters, indicated by the dotted ellipses. The symbols indicate the heat-treatment temperature, and it can be seen that, within both clusters, there is a trend towards more negative scores on both PCs as the heat-treatment temperature is increased. We can conclude that the dominant factors determining the shape of the Raman spectra are the composition and the heat-treatment temperature (as would be expected). For the 25CeDT samples, there is nearly no difference between the freeze-dried and hotplate-dried samples. However, for the 50CeDT samples, there are significant differences between the spectra of S9 (50CeFA) and S13 (50CeHA) and also between S10 (50CeF1000) and S14 (50CeH1000). While S14 is grouped with the 50CeD1100 and 50CeD1200 samples, S10 lies in between these samples and the as-prepared ones.

3.2. TPR measurements

Temperature programmed reduction (TPR) in hydrogen gas was performed on each of the 16 samples in order to assess the effects
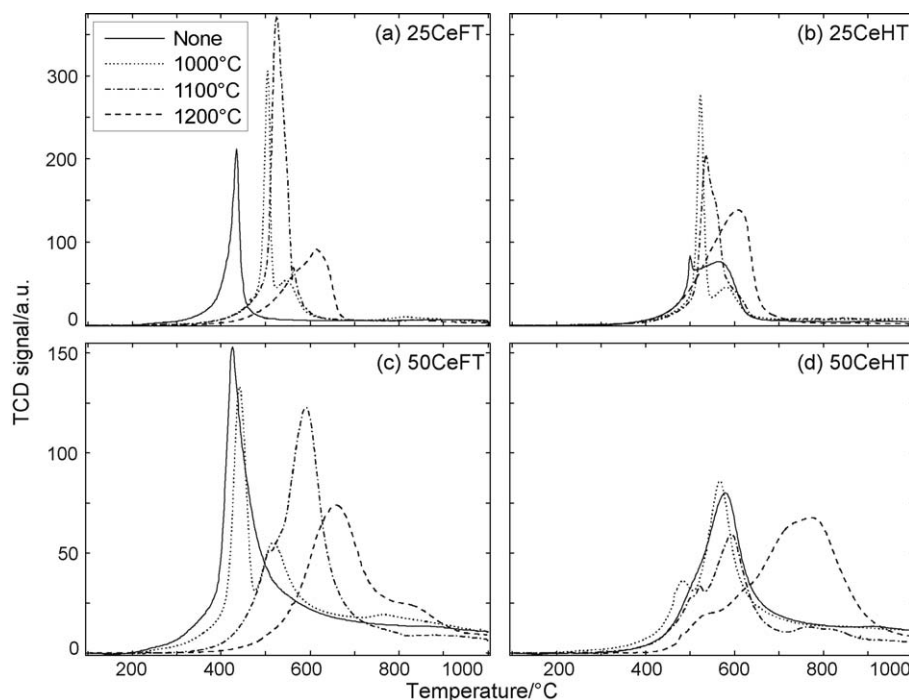
Fig. 7. TPR profiles for as-prepared and heat-treated samples for (a) the 25CeFT series, (b) 25CeHT series, (c) 50CeFT and (d) 50CeHT series. H = hotplate-dried; F = freeze-dried and T = temperature of heat-treatment, either none (solid line), 1000 °C (dotted line), 1100 °C (dot-dash line), or 1200 °C (dashed line).

of synthesis methods and compositions on oxygen lability (Fig. 7). In these experiments, the samples were first heated to 400 °C under oxidizing atmosphere (air) and then switched to a reducing atmosphere (H$_2$) with further heat-treatment up to 1000 °C. TPR peaks due to hydrogen consumption below ca. 550 °C are generally believed to be due to reaction with the lattice oxygen near to surface (hereby referred as surface lattice oxygen), whilst, reduction above ca. 550 °C is usually bulk oxygen [69]. The TPR data showed very different profiles due to the different synthesis and drying parameters used.

The TPR plot for 50CeFA (S9) showed a single broad hydrogen consumption peak centred at ca. 426 °C due to the reduction of surface lattice oxygen (Fig. 7c). By comparison, the analogous 50CeHA sample (S13) showed a single peak centred at ca. 580 °C (Fig. 7d). This difference is unsurprising, since freeze-drying may reduce particle agglomeration, which can increase surface area and surface activity. Furthermore, the temperature of the first "reduction peak" at 426 °C (S9) suggests very labile oxygen. Typically, literature reports for Ce–Zr oxide (CZ) and Ce–Zr–La oxide (CK) materials show this temperature is usually in the range 500–550 °C [59,18]. Again, this is unsurprising given the high surface area (see Table 1) of the as-prepared powders obtained using the CHFS method. The TPR data for 50CeD1000 samples showed two reduction peaks for both 50CeF1000 (S10, peaks at 442 °C and 520 °C, Fig. 7c) and 50CeH1000 (S14, peaks at 484 °C and 567 °C, Fig. 7d) samples. Yet again, a low temperature peak was indicative of surface lattice oxygen reduction and the latter was due to bulk oxygen reduction. Noticeably, for sample 50CeF1000 (S10) the first reduction peak in the TPR plot was centred at a much lower temperature than the corresponding peak for 50CeH1000 (S14), which is unsurprising given the lower BET surface are of the latter (13.8 m^2 g^{-1} versus 6.8 m^2 g^{-1}). The first

TPR reduction peak for the 50CeD1100 and 50CeD1200 samples was located at higher temperatures with respect to the corresponding 50CeD1000 samples; a reduction in the amount of hydrogen consumed was also observed. For 50CeHT samples, the temperature of the first reduction peak in the TPR was always at a higher value than the corresponding 50CeFT samples.

The 25CeFA sample (S1) revealed a sharp first reduction peak in the TPR plot centred at ca. 433 °C (Fig. 7a). This can be compared to a value of 500 °C for 25CeHA sample (S5). After heat-treatment, the TPR plots for the 25CeD1000 samples also contained a sharp peak due to surface lattice oxygen reduction (S2 at 504 °C and S6 at 524 °C) accompanied by a small shoulder (due to bulk lattice oxygen reduction), as shown in Fig. 7b. The retention of surface lattice reduction for the 25CeDT samples is unsurprising given relatively high doping of Zr^{4+} ions, which can result in more surface defects [4,8]. Higher heat-treatment temperatures for the samples (i.e. 25CeD1100 and 25CeD1200), generally resulted in the first reduction peak being found at higher temperature.

The TPR profiles were used to calculate the cumulative hydrogen consumption of all the materials per gram (supplementary Figure S1) or normalised cumulative hydrogen consumption (cumulative hydrogen consumption divided by the BET surface area in m^2 g^{-1} multiplied by the ceria mole fraction) as shown in Fig. 8. In general, the 25CeDT samples showed a steep cumulative hydrogen consumption profile followed by a plateau, whilst the 50CeDT samples showed a much more steady cumulative hydrogen consumption profile. The freeze-dried samples S9 (50CeFA), S10 (50CeF1000) and S1 (25CeFA) showed a particularly low temperature onset of hydrogen consumption, which rises sharply with temperature. All of the 25CeDT samples bar S4 (25CeFA), showed a steep increase in cumulative hydrogen consumption in the range ca. 485–630 °C before a plateau was
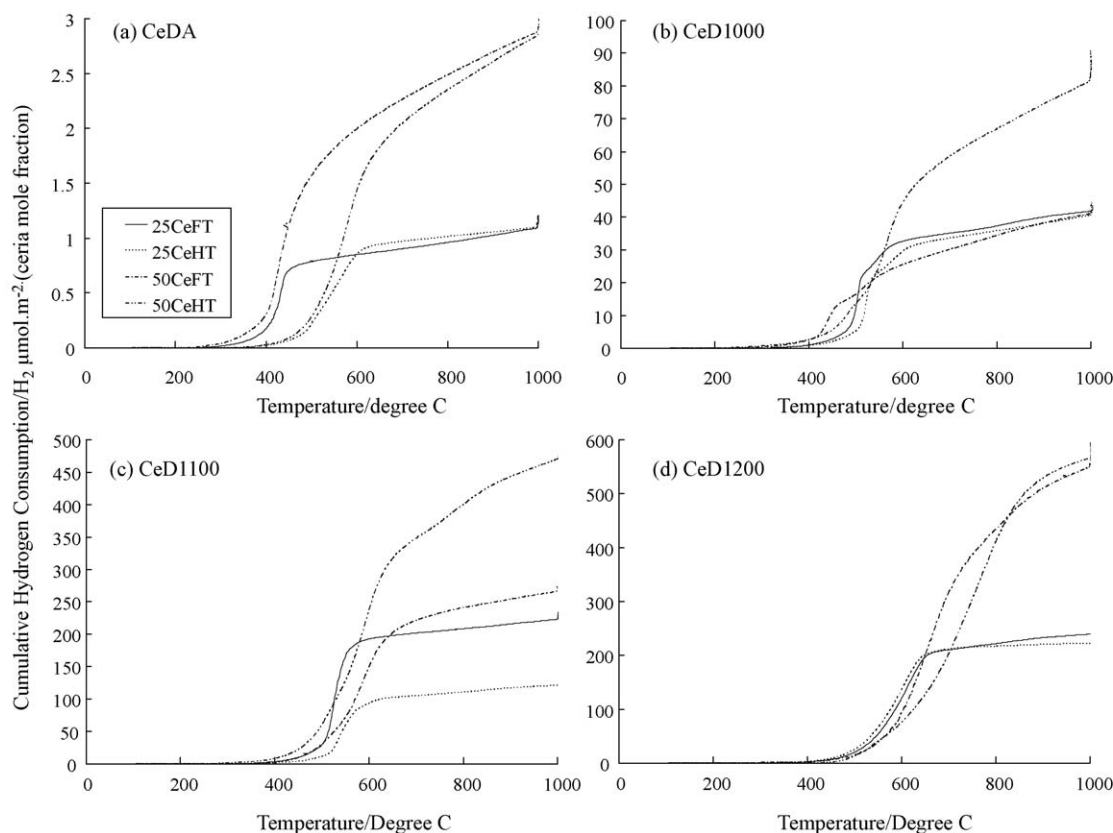

Fig. 8. Cumulative hydrogen consumption for the 25CeDT and 50CeDT samples for (a) the as-prepared samples with no heat-treatment, (b) CeD1000 samples (c) CeD1100 samples and (d) CeD1200 samples. Key: D (drying type) can be either H = hotplate-dried; F = freeze-dried (the temperature for heat-treatment, T = A which is as-prepared, 1000 °C, 1100 °C, or 1200 °C).

reached. Similarly, all except samples S9 (50CeFA) and S10 (50CeF1000) for the 50CeDT set, showed steady rises in the cumulative hydrogen consumption plots above 450 °C (Fig. 8). The cumulative hydrogen consumption for the 50CeDT samples was in the range 1385–1143 μmols g^{-1} (see supplementary Figure S1), corresponding to a normalised range of 3.1–494.6 H$_2$ μmols m^{-2}(ceria mole fraction) of hydrogen gas (at 1000 °C in the TPR, see Fig. 8), whilst the corresponding values for the 25CeDT samples was in the range 989–870 μmols g^{-1} (see supplementary Figure S1), corresponding to a range of 1.3–292.6 H$_2$ μmols m^{-2}(ceria mole fraction) of hydrogen gas (see Fig. 8). These values are considered to be consistent with other work reported elsewhere [13,18,59,11]. Interestingly, heat-treatment of samples to 1000 °C or 1100 °C, often resulted in increased cumulative hydrogen consumption (at 1000 °C in the TPR) although heat-treatment at 1200 °C usually resulted in lower values, which is most likely due to the deleterious effects of sintering and loss of surface area (see supplementary Figure S1).

In order to explain the differences in total hydrogen consumption between samples, selected materials were analyzed using X-ray photoelectron spectroscopy (XPS), which can give useful insights into surface species. The XPS spectrum for the 50CeFA sample (S9) revealed a mixture of Ce^{3+} and Ce^{4+} oxidation states, with the latter dominating (Fig. 9a). The XPS data for the corresponding heat-treated samples (S10 and S11) are consistent with a pure Ce^{4+} phase with no evidence for Ce^{3+} species. In tandem with Ce^{3+} oxidation, a clear enrichment of La^{3+} at the surface was observed after heat-treatment, e.g. approximately a two-fold increase for S11 (50CeF1100) compared to S9 (50CeFA, see Fig. 9b and Table 2). This suggests that the increased total hydrogen consumption (at 1000 °C in the TPR) might be correlated to the increased segregation of La^{3+} to the surface with increasing post synthesis heat-treatment temperature. Furthermore, heating to 1100 °C leads to a marked increase in surface Zr content compared

Table 2
XPS derived surface metal compositions for samples S9, S10 and S11. The EDAX (bulk) analysis of sample S9 is also shown for comparison (standard deviation for atomic ratios are ca. ± 0.01).

Sample	Technique	Heat-treatment	Atomic ratio			
			Ce	Zr	La	Y
S9	EDAX	None	0.50	0.39	0.04	0.07
S9	XPS	None	0.49	0.36	0.05	0.10
S10	XPS	1000 °C	0.44	0.37	0.09	0.10
S11	XPS	1100 °C	0.33	0.45	0.10	0.12

with the sample treated at 1000 °C, and a concomitant, ca. 25 %, decrease in the population of surface Ce species (Table 2) [70]. The corresponding Y(3d) spectra exhibit a broad peak envelope, with the Y(3d$_{3/2}$) Y(3d$_{5/2}$) peaks almost equally intense (Fig. 9c). This indicated the presence of at least two species. Curve fitting analysis revealed Y(3d$_{5/2}$) signals at 156.5 and 158.6 eV, where the former binding energy species was characteristic of Y$_2$O$_3$ [71] and the latter was seemingly characteristic of non-stoichiometric species, which decreased after ageing in air. From consideration of the inelastic background "step", it seems the yttria is very much a surface species, with the other metals distributed more within the surface region. It should be noted that EDX confirmed that the overall elemental compositions are identical after heat-treatments (within instrumental error), and hence the segregation effects seen in XPS are real.

In addition, the Y spectra were curve fitted as they showed interesting changes. The La spectra did not change, other than in concentration, so curve-fitting was deemed unnecessary. With regard to the Ce data, due to the uncertainty in the curve-fitting procedure arising from the complexity of the spectral envelope, it was considered that the presence of Ce^{3+} be estimated by comparing the shape of the recorded spectra with that of reference [73].
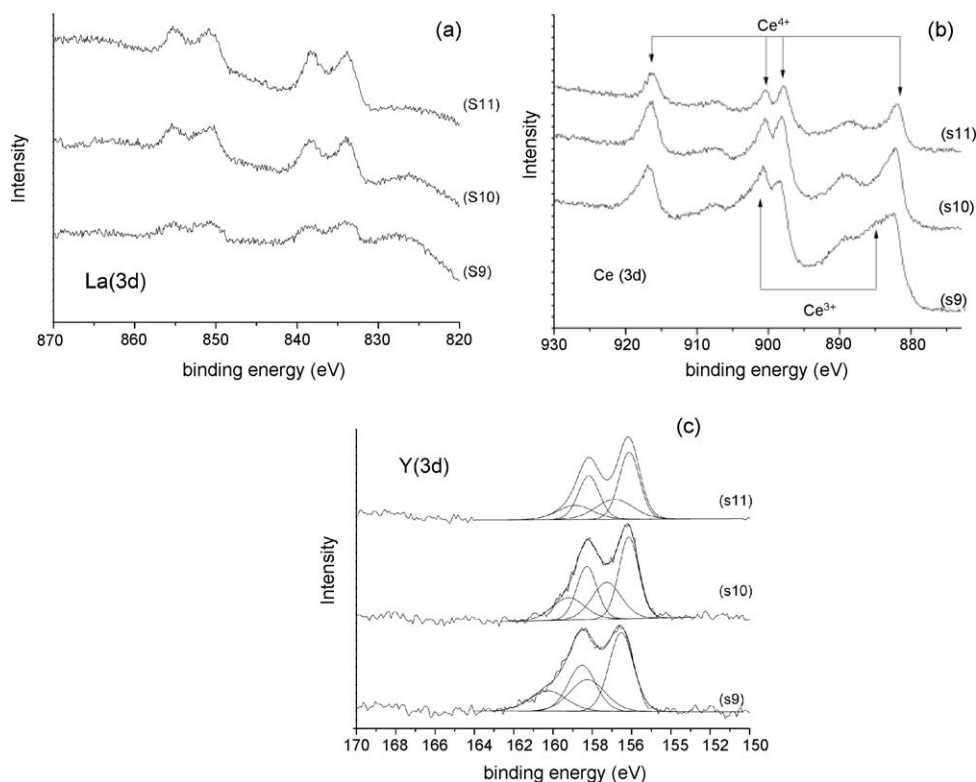

Fig. 9. XPS spectra for 50CeFA (S9), 50CeF1000 (S10) and 50CeF1100 (S11), where (a) Ce(3d) XPS spectra indicating the presence of Ce^{3+} and Ce^{4+} with the Ce^{4+} state dominating with increasing annealing temperature, (b) La(3d) XPS spectra the enrichment of La^{3+} at the surface and (c)Y(3d) XPS spectra, indicating the presence of two species, of which the higher binding energy species decreases with increasing temperature.

In the O(1s) spectra, there is a continuous decrease in the intensity of a high binding energy shoulder with heat-treatment – this could be due to a decrease in defects and the associated O_x^- species. Further, XPS was sufficiently sensitive to suggest that there is a very small amount of Fe present (<1 at%) in all samples. This was not surprising, as we did not use any special corrosion resistant alloys in our counter-current mixers (instead we used stainless steel due to low cost and convenience).

The redox percentages (actual/theoretical conversion of all Ce^{4+} to Ce^{3+} at 1000 °C) for the samples are presented in Table 1, and suggested that the 25CeDT samples performed relatively better than the 50CeDT samples as expected. Surprisingly, such redox properties even improved after ageing, presumably due to the greater segregation of La^{3+} at the surface (as suggested in the XPS), which may act to increase the total amount of available oxygen.

3.3. Colour measurements

The samples were analyzed using UV/Vis spectroscopy in diffuse reflectance mode. Colour coordinates for the 16 samples were calculated from these data and are presented in Fig. 10. All of the 25CeDT samples were located in the yellow–green region whilst most of 50CeDT samples were located in the yellow–red region. This is unsurprising given that the 50CeDT samples contain more Ce^{4+} (yellow). Furthermore, the four as-prepared samples all showed relatively high yellow colour, also suggesting the presence of high amounts of Ce^{4+} cations, which is consistent with the literature [60]. In comparison, samples 25CeD1000 and 50 CeD1000 were light yellow, indicating an increase in Ce^{3+} (colourless) content. This can be correlated to the corresponding TPR results, which showed an increase of the total hydrogen consumption (at 1000 °C) compared to the as-prepared analogues. The XPS spectrum for 50CeF1000 sample (S10) revealed the Ce^{4+} oxidation state was predominant at the surface of the sample, which is expected as the vast majority of the ceria is still in the 4+ state.

Increasing the ageing temperature for the freeze-dried sample 50CeF1100 (S11) resulted in a more yellow sample than 50CeF1000 (S10) indicating a decrease of Ce^{3+}. In contrast, the hotplate-dried sample 50CeH1100 (S15) was less yellow than 50CeH1000 (S14). By comparison, a pure CeO_2 sample made using the CHFS method has a colour of pale yellow ($L_0 = 87.35$, $a = 0.73$, $b = 16.98$). For the 25CeDT powders, the freeze-dried sample 25CeF1100 (S3) was less yellow than 25CeF1000 (S2), whilst in the case of the hotplate-dried samples 25CeH1100 (S7) and 25CeH1000 (S6), this trend was reversed. All of these observations are consistent with the TPR data in that the lighter the yellow

colour of the sample, the higher the total hydrogen consumption (at 1000 °C).

When the samples were aged at 1200 °C, sample colours were strongly affected by the severe sintering, e.g. the 25CeD1200 samples, S4 and S8, possessed greener colour than all the other 25CeDT samples. Sample 50CeH1200 (S16), possessed more red colour than the other 50CeDT samples, whilst sample 50CeF1200 (S12) was light yellow. As before, the colour data were generally consistent with the TPR data in that the lighter the yellow colour of the sample, the higher the total hydrogen consumption (at 1000 °C). Thus, we have clearly shown the total hydrogen consumption values can be correlated well with the colour of the samples as expected.

3.4. Chemometric methods

Since TPR experiments are very time-consuming, it is desirable to develop faster and perhaps indicative tests that can be used for screening as part of a high-throughput catalyst materials development programme. Thus, we looked for correlations between the Raman results and the performance metrics derived from the TPR data. The specific performance metrics chosen were the first reduction peak temperature (at which the maximum TCD signal occurs) and the cumulative H_2 consumption at 500, 750 and 1000 °C. A low peak temperature was of course desirable, as was high H_2 consumption, with consumption at lower temperatures being particularly of interest. It should be noted that misleading calibration results can be obtained when using heterogeneous datasets. For example, in the present case, the 50CeDT materials naturally have greater H_2 consumption than the 25CeDT ones; they also have different Raman spectra. A model calibrated using the full dataset can provide apparently good results simply by separating the two groups of samples and assigning approximately the mean performance of each group to all members of that group. Such a model performs fairly well in cross-validation, but would have little generalization ability. For this reason we have not attempted calibrations for the H_2 consumption measures with the full dataset, reducing the number of calibration problems to the eight listed in Table 3.

We used principal component regression (PCR), in which the principal components were used as predictor variables in multiple linear regression [68]. The number of principal components was varied from 1 to 4 and models were built with and without pre-processing by intensity normalization. The optimal pre-treatment and number of principal components were chosen to minimize the root mean square error of cross-validation (RMSECV) [68]. Because of the limited amount of data and the risk of overfitting, we have not attempted extensive model optimization or the use of more flexible models such as artificial neural networks or support vector machines.

The results of the modeling are presented in Table 3, and the cross-validation results of the peak-reduction-temperature model
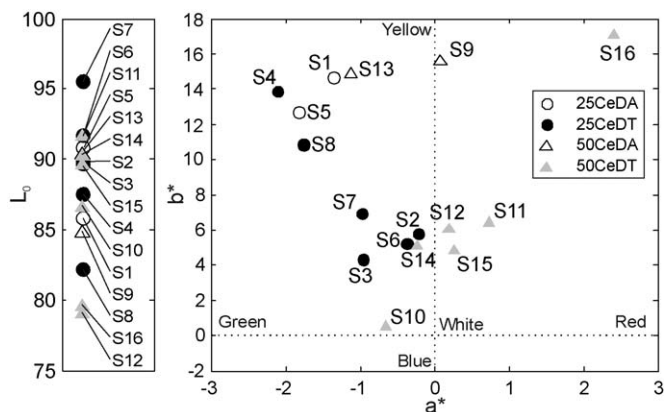

Fig. 10. L_0, a^* and b^* colour coordinates (in the CIE LAB space) for all the Ce–Zr–La–Y oxide samples.

Table 3
Cross-validation results for PCR models predicting performance measures from Raman spectra. Norm indicates whether normalization was used; A is the number of principal components (chosen to minimize the RMSECV); E is the RMSECV as a percentage of the range of the target variable; p is the percentile of E in the RMSECV distribution obtained in the randomization test (see text); and R^2 is the coefficient of determination (which may be negative in cross-validation).

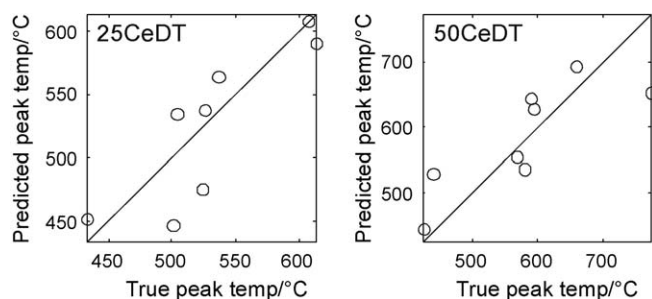|	25CeDT				50CeDT			
	Norm	A	E (p)	R^2	Norm	A	E	R^2
Peak temperature	No	4	18 (0.0)	0.66	Yes	2	18 (0.0)	0.66
H_2 (500 °C)	Yes	3	25 (0.5)	0.37	Yes	4	12 (1.1)	0.86
H_2 (750 °C)	No	3	19 (0.0)	0.67	No	2	29 (0.0)	0.03
H_2 (1000 °C)	Yes	1	30 (9.0)	−0.05	Yes	1	31 (0.0)	−0.19

Fig. 11. Cross-validation results for the position of the low temperature reduction peak in the TPR predicted from Raman spectra for (a) 25CeDT and (b) 50CeDT samples. The PCR models used data from as-measured TPR plots and normalized spectra are 2 and 3 principal components for the 25CeDT and 50CeDT datasets, respectively.

are plotted in Fig. 11. The significance of each model was assessed by a randomization test in which the cross-validation was repeated with 10,000 random permutations of the response values. This procedure generates a distribution of RMSECV values that could be expected if there were no relationship between the predictor and response variables. The percentile p of the actual RMSECV within this distribution is an indicator of the statistical significance of the model. Generally, we found that models with some predictive ability ($p < 5\%$) were obtained (with the exception of the cumulative H_2 consumption at 750 °C). These results are encouraging, and suggest that chemometric models based on rapid spectroscopic measurements could be useful in future high-throughput investigations. We anticipate that a larger body of data would of course allow for better model calibration and validation, and also for the use of more sophisticated modeling methods.

4. Conclusions

A continuous hydrothermal flow synthesis system was used to make candidate solid solutions as crystalline nanopowders using a superheated water feed at 450 °C and 24.1 MPa that reacts with the appropriate metal salts in solution. The conditions for drying of slurries and the heat-treatment of samples appeared in certain cases to have a significant effect on the final properties such as surface area and total oxygen storage capacity of the powders. The total hydrogen consumption of the materials was generally high. In selected cases, the materials possessed labile surface lattice oxygen at low temperatures. This is important when we consider that the materials do not contain any precious metals, which would of course significantly lower the temperature yet further.

Accelerated ageing tests conducted at different temperatures had a significant effect on the total OSC and low temperature labiality of oxygen in the materials. Significantly, the 50CeF1000 sample (S10) resulted in a higher than expected surface area of 13.8 $m^2 g^{-1}$ and this sample showed unusually high total hydrogen consumption at 1000 °C and a low peak temperature in the TPR. Interestingly, the sample colour was also very different to the other samples, being almost white, suggesting the presence of significant amounts of Ce^{3+} in the lattice.

As the development of better TWC materials is a very complex and multidimensional materials problem, and because the measurement of important properties such as OSC can be considered as a bottleneck, the authors are sought to find more rapid and indicative methods for developing better TWCs. The possible correlation of spectroscopic or related probes to these important properties was investigated. The results suggest that this approach is promising, but more work and data are required to validate the findings. Towards these goals, high-throughput synthesis and screening methods need to be developed. Indeed

such approaches to high-throughput CHFS reactors have recently been developed [72].

Appendix A. Supplementary data

Supplementary data associated with this article can be found, in the online version, at doi:10.1016/j.apcatb.2009.03.031.

References

[1] J. Kaspar, R.D. Monte, P. Fornasiero, M. Graziani, H. Bradshaw, C. Norman, Top. Catal. 16 (2001) 83–87.
[2] M.P. Walsh, Am. J. Ind. Med. 50 (2007) 853–860.
[3] H.S. Gandhi, K. Otto, A.G. Piken, M. Shelef, Abstr. Pap. Am. Chem. Soc. 172 (1976) 36–136.
[4] D. Duprez, C. Descorme, T. Birchem, E. Rohart, Top. Catal. 16 (2001) 49–56.
[5] T.N. Angelidis, Top. Catal. 16 (2001) 419–423.
[6] M. Ozawa, J. Alloys Compd. 275–277 (1998) 886–890.
[7] Vehicle Standards and Regulations, http://www.epa.gov/otaq/standards.htm (2007).
[8] P. Fornasiero, R. Dimonte, G.R. Rao, J. Kaspar, S. Meriani, A. Trovarelli, M. Graziani, J. Catal. 151 (1995) 168–177.
[9] A. Cabanas, J.A. Darr, E. Lester, M. Poliakoff, Chem. Commun. 11 (2000) 901–902.
[10] A. Cabanas, J.A. Darr, E. Lester, M. Poliakoff, J. Mater. Chem. 11 (2001) 561–568.
[11] A. Morikawa, T. Suzuki, T. Kanazawa, K. Kikuta, A. Suda, H. Shinjo, Appl. Catal., B: Environ. 78 (2008) 210–221.
[12] Z.X. Song, W. Liu, H. Nishiguchi, A. Takami, K. Nagaoka, Y. Takita, Appl. Catal., A – Gen. 329 (2007) 86–92.
[13] X. Wu, X. Wu, Q. Liang, J. Fan, D. Weng, Z. Xie, S. Wei, Solid State Sci. 9 (2007) 636–643.
[14] G. Dell Agli, G. Mascolo, J. Eur. Ceram. Soc. 24 (2004) 915–918.
[15] J. Mikulova, S. Rossignol, F. Gerard, D. Mesnard, C. Kappenstein, D. Duprez, J. Solid State Chem. 179 (2006) 2511–2520.
[16] S. Rossignol, C. Descorme, C. Kappenstein, D. Duprez, J. Mater. Chem. 11 (2001) 2587–2592.
[17] Z.B. Yang, P.Y. Lin, W.D. Wang, S.M. Yu, Chin. J. Catal. 22 (2001) 365–369.
[18] J. Fan, X. Wu, X. Wu, Q. Liang, R. Ran, D. Weng, Appl. Catal., B: Environ. 81 (2008) 38–48.
[19] A. Trovarelli, F. Zamar, J. Llorca, C.D. Leitenburg, G. Dolcetti, J.T. Kiss, J. Catal. 169 (1997) 490–502.
[20] S. Rossignol, Y. Madier, D. Duprez, Catal. Today 50 (1999) 261–270.
[21] K. Yamashita, K.V. Ramanujachary, M. Greenblatt, Solid State Ionics 81 (1995) 53–60.
[22] A.P. Oliveira, M.L. Torem, Powder Technol. 119 (2001) 181–193.
[23] F.C. Gennari, T. Montini, P. Fornasiero, J.J. Andrade Gamboa, Int. J. Hydrogen Energy 33 (2008) 3549–3554.
[24] V. Grover, S.V. Chavan, P.U. Sastry, A.K. Tyagi, J. Alloys Compd. 457 (2008) 498–505.
[25] S.T. Aruna, K.C. Patil, Nanostruct. Mater. 10 (1998) 955–964.
[26] W. Chen, F. Li, J. Yu, L. Liu, H. Gao, Mater. Res. Bull. 41 (2006) 2318–2324.
[27] F.E. Ghodsi, F.Z. Tepehan, G.G. Tepehan, Sol. Energy Mater. Sol. Cells 92 (2008) 234–239.
[28] Q. Long, M. Cai, J.D. Rogers, H.L. Rong, J.R. Li, L. Jiang, Nanotech. 18 (2007) 6–10.
[29] N.N. Gavrilova, O.V. Zhilina, V.V. Nazarov, Russ. J. Appl. Chem. 80 (2007) 1468–1471.
[30] J. Kaspar, P. Fornasiero, J. Solid State Chem. 171 (2003) 19–29.
[31] J.A. Darr, M. Poliakoff, Abstr. Pap. Am. Chem. Soc. 216 (1998) U648–U1648.
[32] A.A. Chaudhry, S. Haque, S. Kellici, P. Boldrin, I. Rehman, A.K. Fazal, J.A. Darr, Chem. Commun. (2006) 2286–2288.
[33] P. Boldrin, A.K. Hebb, A.A. Chaudhry, L. Otley, B. Thiebaut, P. Bishop, J.A. Darr, Ind. Eng. Chem. Res. 46 (2007) 4830–4838.
[34] X. Weng, P. Boldrin, I. Abrahams, S.J. Skinner, J.A. Darr, Chem. Mater. 19 (2007) 4382–4384.
[35] X. Weng, P. Boldrin, I. Abrahams, S.J. Skinner, S. Kellici, J.A. Darr, J. Solid State Chem. 181 (2008) 1123–1132.
[36] J.A. Darr, M.A. Poliakoff, W.S. Li, A.J. Blake, J. Chem. Soc., Dalton Trans. (1997) 2869–2874.
[37] J.A. Darr, M. Poliakoff, A.J. Blake, W.S. Li, Inorg. Chem. 37 (1998) 5491–5496.

[38] J.A. Darr, M. Poliakoff, Chem. Rev. 99 (1999) 495–541.
[39] K. Gong, R. Viboonkiat, I.U. Rehman, G. Buckton, J.A. Darr, J. Pharm. Sci. 94 (2005) 2583–2590.
[40] K. Gong, J.A. Darr, I.U. Rehman, Int. J. Pharm. 315 (2006) 93–98.
[41] S. Partap, I. Rehman, J.R. Jones, J.A. Darr, Adv. Mater. 18 (2006) 501–506.
[42] K. Gong, I.U. Rehman, J.A. Darr, Int. J. Pharm. 338 (2007) 191–197.
[43] K. Gong, M. Braden, M.P. Patel, I.U. Rehman, Z. Zhang, J.A. Darr, J. Pharm. Sci. 96 (2007) 2048–2056.
[44] E.N. Gribov, E.V. Parkhomchuk, I.M. Krivobokov, J.A. Darr, A.G. Okunev, J. Membr. Sci. 297 (2007) 1–4.
[45] S. Partap, A.K. Hebb, I.U. Rehman, J.A. Darr, Polym. Bull. 58 (2007) 849–860.
[46] G.J. Hutchings, J.A. Lopez-Sanchez, J.K. Bartley, J.M. Webster, A. Burrows, C.J. Kiely, A.F. Carley, C. Rhodes, M. Havecker, A. Knop-Gericke, R.W. Mayer, R. Schlogl, J.C. Volta, M. Poliakoff, J. Catal. 208 (2002) 197–210.
[47] Z.R. Tang, J.K. Edwards, J.K. Bartley, S.H. Taylor, A.F. Carley, A.A. Herzing, C.J. Kiely, G.J. Hutchings, J. Catal. 249 (2007) 208–219.
[48] T. Adschiri, K. Kanazawa, K. Arai, J. Am. Ceram. Soc. 75 (1992) 1019–1022.
[49] M. Watanabe, T. Adschiri, K. Arai, Kobunshi Ronbunshu 58 (2001) 631–641.
[50] M. Watanabe, M. Mochiduki, S. Sawamoto, T. Adschiri, K. Arai, J. Supercrit. Fluids 20 (2001) 257–266.
[51] M. Sasaki, T. Adschiri, K. Arai, Bioresour. Technol. 86 (2003) 301–304.
[52] M. Watanabe, H. Inomata, M. Osada, T. Sato, T. Adschiri, K. Arai, Fuel 82 (2003) 545–552.
[53] M. Osada, M. Watanabe, K. Sue, T. Adschiri, K. Arai, J. Supercrit. Fluids 28 (2004) 219–224.
[54] M. Atashfaraz, M. Shariaty-Niassar, S. Ohara, K. Minami, M. Umetsu, T. Naka, T. Adschiri, Fluid Phase Equilib. 257 (2007) 233–237.
[55] D. Rangappa, S. Ohara, M. Umetsu, T. Naka, T. Adschiri, J. Supercrit. Fluids 44 (2008) 441–445.
[56] T. Adschiri, K. Kanazawa, K. Arai, J. Am. Ceram. Soc. 75 (1992) 2615–2618.
[57] Y. Hakuta, K. Seino, H. Ura, T. Adschiri, H. Takizawa, K. Arai, J. Mater. Chem. 9 (1999) 2671–2674.
[58] Y. Hakuta, T. Adschiri, H. Hirakoso, K. Arai, Fluid Phase Equilib. 160 (1999) 733–742.
[59] J.R. Kim, W.J. Myeong, S.K. Ihm, Appl. Catal., B: Environ. 71 (2007) 57–63.
[60] R. Si, Y.W. Zhang, L.M. Wang, S.J. Li, B.X. Lin, W.S. Chu, Z.Y. Wu, C.H. Yan, J. Phys. Chem. 111 (2007) 787–794.
[61] A.C. Larson, R.B. Von Dreele, Los Alamos Natl. Lab. Rep. LAUR (1986) 748.
[62] E. Lester, P. Blood, J. Denyer, D. Giddings, B. Azzopardi, M. Poliakoff, J. Supercrit. Fluids 37 (2006) 209–214.
[63] M.J. Phillips, J.A. Darr, Z.B. Luklinska, I. Rehman, J. Mater. Sci. - Mater. Med. 14 (2003) 875–882.
[64] H. Vidal, J. Kaspar, M. Pijolat, G. Colon, S. Bernal, A. Cordon, V. Perrichon, F. Fally, Appl. Catal., B: Environ. 27 (2000) 49–63.
[65] B.M. Reddy, A. Khan, Proc. Catal. Surv. Asia 9 (2005) 155–171.
[66] B.M. Reddy, A. Khan, P. Lakshmanan, M. Aouine, S. Loridant, J.C. Volta, J. Phys. Chem. B 109 (2005) 3355–3363.
[67] B.P. Mandal, V. Grover, M. Roy, A.K. Tyagi, J. Am. Ceram. Soc. 90 (2007) 2961–2965.
[68] R.G. Brereton, Chemometrics: Data Analysis For The Laboratory and Chemical Plant, John Wiley & Sons, Chichester, UK, 2003.
[69] F. Fally, V. Perrichon, H. Vidal, J. Kaspar, G. Blanco, J.M. Pintado, S. Bernal, G. Colon, M. Daturi, J.C. Lavalley, Catal. Today 59 (2000) 373–386.
[70] F. Zhang, S.W. Chan, J.E. Spanier, E. Apak, Q. Jin, R.D. Robinson, I.P. Herman, Appl. Phys. Lett. 80 (2002) 127–129.
[71] A.E. Hughes, B.A. Sexton, J. Mater. Sci. 24 (1989) 1057–1061.
[72] X. Weng, J.K. Cockcroft, G. Hyett, M. Vickers, P. Boldrin, C.C. Tang, S.P. Thompson, J.E. Parker, J.C. Knowles, I. Rehman, I. Parkin, J.R.G. Evans, J.A. Darr, J. Combi. Chem. Soc. 2009 under review.
[73] E. Beche, P. Charvin, D. Perarnau, S. Abanades, G. Flamant, Surf. Interface. Anal. 40 (2008) 264–267, references therein.